ADVANCED INTELLIGENT SYSTEMS
Open Access
www.advintellsyst.com

Bio-to-Robot Transfer of Fish Sensorimotor Dynamics via Interpretable Model

Waqar Hussain Afridi, Ahsan Tanveer, Rahdar Hussain Afridi, Muhammad Hamza, Mingxin Wu, Liang Li, and Guangming Xie**

Swimming in fish arises from tightly integrated neural, muscular, skeletal, and hydrodynamic processes that are difficult to capture in compact, transferable models for robotics. An interpretable system identification (SySID) is presented that bidirectionally maps between electromyography (EMG) and kinematics in freely swimming koi and further tests its generalization to a robotic fish. Synchronized EMG and kinematic are collected across laminar, Kármán vortex, and reverse Kármán vortex flows spanning 0.146–0.274 m s^{-1}. A linear autoregressive with exogenous input (ARX) model architecture is chosen to capture both feedforward (EMG to kinematics) and feedback (kinematics to EMG) pathways, enabling the extraction of key system parameters, such as natural frequency, damping ratio, and input–output delays. Cross-individual validation demonstrates robust performance and identifies the best-performing fish-trained model, which is then evaluated for cross-domain transfer by replacing EMG input with processed pulse width modulation actuation signals from a robotic fish. Despite differences in mechanics and actuation physics, predictions closely match measured trajectories (mean $R^2 = 0.86 \pm 0.13$), substantially outperforming a deep neural network (97.8% higher percentage fit index) trained on the same biological datasets. These findings show that compact, interpretable SySID models enable accurate bio-to-robot transfer without robot-specific retraining, grounding robotic motion models directly in biological function rather than imitation.

1. Introduction

Evolution has equipped fish with locomotion systems capable of high propulsive efficiency, rapid acceleration, and maneuverability, making bioinspiration a productive route for motion design in water.[1–4] Swimming in aquatic animals emerges from the flexible body and flow interactions that can even yield efficiency through vortex exploitation by an integrated sensorimotor system responsive to body state and external conditions.[5–10] The governing mechanics of aquatic locomotion are high-dimensional and nonlinear, spanning actuation, material properties, and hydrodynamics, and they inform motion models and design methods that exploit morphology and compliance. Bioinspired engineering seeks to translate these principles into robotic platforms and materials, yet while external features such as soft actuators, compliant joints, and streamlined bodies are readily reproduced, capturing the adaptive sensorimotor dynamics remains a major challenge.[11–13] This challenge is

W. H. Afridi, A. Tanveer, R. H. Afridi, M. Hamza, M. Wu, G. Xie
College of Engineering
Intelligent Biomimetic Design Lab
School of Advanced Manufacturing and Robotics
Peking University
Beijing 100871, China
E-mail: xiegming@pku.edu.cn

W. H. Afridi, A. Tanveer, R. H. Afridi, M. Hamza, M. Wu, G. Xie
State Key Laboratory for Turbulence and Complex Systems
College of Engineering, Peking University, China
Beijing 100871, China

M. Wu
School of Mechanics and Safety Engineering
Zhengzhou University
Zhengzhou 450001, China

The ORCID identification number(s) for the author(s) of this article can be found under https://doi.org/10.1002/aisy.202501117.

DOI: 10.1002/aisy.202501117

L. Li
Department of Collective Behaviour
Max Planck Institute of Animal Behavior
78464 Konstanz, Germany
E-mail: lli@ab.mpg.de

L. Li
Centre for the Advanced Study of Collective Behaviour
University of Konstanz
78467 Konstanz, Germany

L. Li
Department of Biology
University of Konstanz
78464 Konstanz, Germany

L. Li
Department of Computer and Information Science
University of Konstanz
78464 Konstanz, Germany

G. Xie
Institute of Ocean Research
Peking University
Beijing 100871, China

essentially to represent biological sensorimotor dynamics in a compact, transferable form that supports robotic motion design.

Despite advances in mimicking external morphology, many bioinspired robots' central pattern generator (CPG) tuning still relies on simplified schemes such as coupled oscillators, rule-based logic, or artificial CPGs.[14–17] While effective for generating stable rhythmic outputs, these approaches rarely incorporate real biological data and often overlook the complex sensorimotor loops essential for adaptive locomotion. Even biologically inspired CPGs, modeled on animal neural circuits for swimming or walking, typically use mathematical oscillators such as coupled Hopf or phase models rather than replicating actual neural or anatomical structures.[18] Recent work with spiking neural networks and neuromorphic architectures modeled on the lamprey spinal cord[19] shows promise, but remains limited in complexity and largely decoupled from in vivo signals. Crucially, no robotic platform has implemented a biologically derived, dynamics-relevant model trained directly from electromyography (EMG) of the target species and transferred to a robot without retraining. This absence of biologically grounded, transferable models constrains both the behavioral realism of bioinspired robots and our broader understanding of animal locomotion, underscoring the need for alternative modeling frameworks rooted in actual biological function.

System identification (SySID) offers a data-driven alternative, extracting dynamic input–output relationships directly from empirical data without requiring detailed biophysical models. SySID methods have already demonstrated substantial utility across diverse biological domains. In human sensorimotor systems, EMG has been linked to kinematics using autoregressive with exogenous input (ARX), nonlinear autoregressive (NARX), and state-space frameworks,[20–22] which naturally incorporate temporal dynamics and feedback loops in interpretable forms. In neural applications, ARX and time-varying ARX have powered electroencephalogram (EEG)-based brain–computer interfaces,[22–24] while multiscale ARX has quantified cortical–subthalamic information transfer in rodent models of Parkinson's disease.[25] Similar methods in conscious sheep have characterized the closed-loop baroreflex and vascular system under independent baroreceptor perturbations.[26] These examples demonstrate that SySID-based modeling schemes, particularly ARX, can be applicable across species and physiological systems, from neurophysiology to cardiovascular systems. Similarly, NARX has revealed nonlinear causal interactions in neural circuits,[27] and state-space models have captured spike-train dynamics and transient oscillations in primate and human recordings.[28,29] Frequency-domain SySID has shown adaptive proprioceptive reweighting in human postural regulation.[28] In aquatic locomotion research, fish EMG is a direct measure of muscle activation patterns driving body curvature; when combined with kinematics, it offers a complete input–output dataset ideally suited for SySID modeling of swimming.

Among all the aforementioned approaches, we focus on the ARX model for its qualities (such as ease of implementation, low computational cost, and interpretability) that make it especially suitable for extracting biologically meaningful structure from complex sensorimotor datasets. Compared to NARX, high-order state-space models, or deep neural networks (DNNs), ARX requires fewer parameters, reducing the risk of overfitting with the limited datasets typical of free-swimming animal experiments, while still enabling recovery of key dynamics-relevant parameters such as natural frequency, damping ratio, and delay.

In addition to extracting meaningful structures from complex biological datasets, there has been significant recent interest in cross-domain modeling, where computational models trained on biological data are directly transferred to robotic platforms.[30] Early work by Nicolelis et al. demonstrated neural-to-robot interfaces in which cortical signals from primates were applied to robotic limbs in real time.[31] More recent efforts have used an EEG decoded by deep learning to achieve cross-subject generalization in a robotic exoskeleton.[32] At the same time, EMG has been transferred to prosthetics and wearable robots in human applications.[33] However, applications of these principles from nonhuman species to robotic platforms remain rare, with notable exceptions such as Montoya et al. who used human EMG-derived signals for a robotic-fish motion modeling framework, demonstrating cross-species, albeit not fully biologically grounded, domain transfer.[34] These successes in other domains underscore the missed opportunity in aquatic vertebrate robotics. To our knowledge, no prior work has demonstrated direct cross-domain transfer of empirically derived sensorimotor dynamics from aquatic vertebrates to robotic fish. This gap persists due to challenges in morphology mismatch, differences in actuation mechanisms, environmental variability, biological signal noise, and the data demands of complex models prone to overfitting.[32]

To address the aforementioned challenges, we present a biologically grounded cross-domain modeling framework that learns the sensorimotor dynamics of freely swimming koi fish. We fit a low-order ARX model to differential EMG and tail displacement (TD) collected across laminar, Kármán, and reverse-Kármán flow regimes, yielding a compact representation that estimates delay, steady-state gain, and related dynamic quantities. We assess zero-shot transfer by using processed pulse width modulation (PWM) actuation as an exogenous input to the EMG-trained ARX model and predicting robotic TD offline. Our contributions are threefold: i) a direct biological-to-robotic prediction approach using an interpretable SysID model trained only on fish data; ii) a bidirectional EMG to kinematics mapping that estimates delays and gains to clarify sensorimotor coupling; and iii) evidence of cross-individual and cross-domain generalization, benchmarked against a DNN in offline tests. Together, these results provide a simple route from animal signals to transferable, interpretable motion models for bioinspired robots.

2. Results and Discussion

We recorded bilateral intramuscular EMG from the caudal musculature of freely swimming koi and synchronized these signals with video-derived TD across multiple flow regimes (laminar, Kármán vortex street (KVS), reverse KVS (RKVS)) and swimming speeds (**Figure 1**, Experimental Section). EMG was rectified and smoothed to obtain envelopes, then combined as a left–right differential and paired with TD to form input–output sequences (**Figure 2**A–C, Experimental Section). We trained a low-order, interpretable ARX model on these fish datasets to predict TD from differential EMG (**Figure 3**A, Experimental Section), selected a single fish-trained model that generalized across

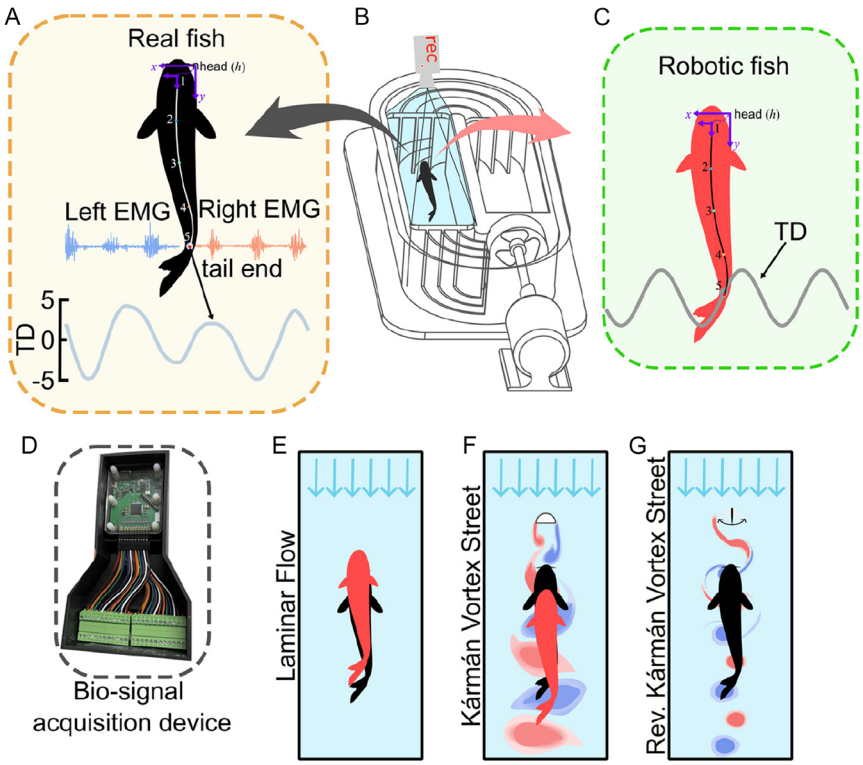

Figure 1. Experimental setup and flow conditions for real and robotic-fish trials. A) Real fish: bilateral EMG from caudal red muscle and TD from video. B) Flow tunnel for real/robotic trials. C) Robotic fish with an open-loop CPG controller. D) Wireless EMG acquisition device. E–G) Flow regimes: laminar, KVS, and RKVS. Only laminar flow was used for robotic trials.

individuals, and diagnostics included representative traces and residual checks (Figure 3B–G). We collected robotic-fish kinematics data (Figure 1A) to generate input-output pairs in laminar and KVS flow regimes (Figure 2D–G) and then applied ARX model to it, without retraining, to a robotic fish to predict robotic TD from processed PWM actuation signals (Figure 3H, Experimental Section). The ARX model revealed system behavior (delay, steady-state gain, and related dynamics) and also real-fish sensorimotor dynamics (**Figure 4**). The ARX model accurately predicted robotic-fish tail motion across varying flow speeds and actuation settings. At the same time, analysis of the real-to-robot body-size ratio revealed that morphological similarity further improved prediction accuracy (**Figure 5**). Performance of ARX models was quantified with coefficient of determination (R^2), percentage fit index (PFI), Pearson's R, root-mean-square error (RMSE, cm), and normalized RMSE (% of max tail amplitude) (**Figure 6**). For context, we also evaluated a trained on the same DNN biological datasets (**Figure 7**) and analyzed simple parameter readouts from the ARX model (delay, steady-state gain, and related dynamics) for interpretability. All analyses are offline; no real-time or closed-loop operation was implemented.

2.1. Cross-Individual ARX Validation

To assess the reproducibility and generalizability of ARX models trained on real-fish data, we implemented a cross-individual validation framework (Figure 3A). Six separate ARX models were trained using differential EMG envelope and TD data from six real-fish datasets, each corresponding to distinct flow conditions and speeds (see **Table 1**). The primary goal of this validation step was twofold: i) to evaluate each model's fidelity in reproducing the dynamics of the dataset it was trained on (self-validation), and ii) to test each model's ability to generalize to unseen fish by applying it to the remaining five datasets (cross-validation, Figure 3B–E).

Model performance was quantified using the R^2, which measures the proportion of variance in the measured output explained by the predicted signal. In addition, RMSE and PFI were computed in later sections to provide complementary assessments of prediction accuracy. Representative examples of self- and cross-validation results are presented in Figure 3B–D, where the ARX model trained on Dataset 1 (Laminar, 0.184 m s^{-1}) shows strong agreement in self-validation ($R^2 = 0.831$), and varying degrees of generalization in cross-validation to Dataset 3 ($R^2 = 0.755$) and Dataset 4 ($R^2 = 0.813$).

A complete summary of cross-validation performance across all six datasets is visualized in Figure 3E, where each row corresponds to a model trained on a specific dataset and each column shows prediction R^2 scores when tested on other datasets. Several trends emerged. First, models trained under laminar flow conditions at 0.184 or 0.274 m s^{-1} tended to generalize better to other laminar datasets compared to RKVS conditions. Notably, the ARX model trained on Dataset 1 achieved

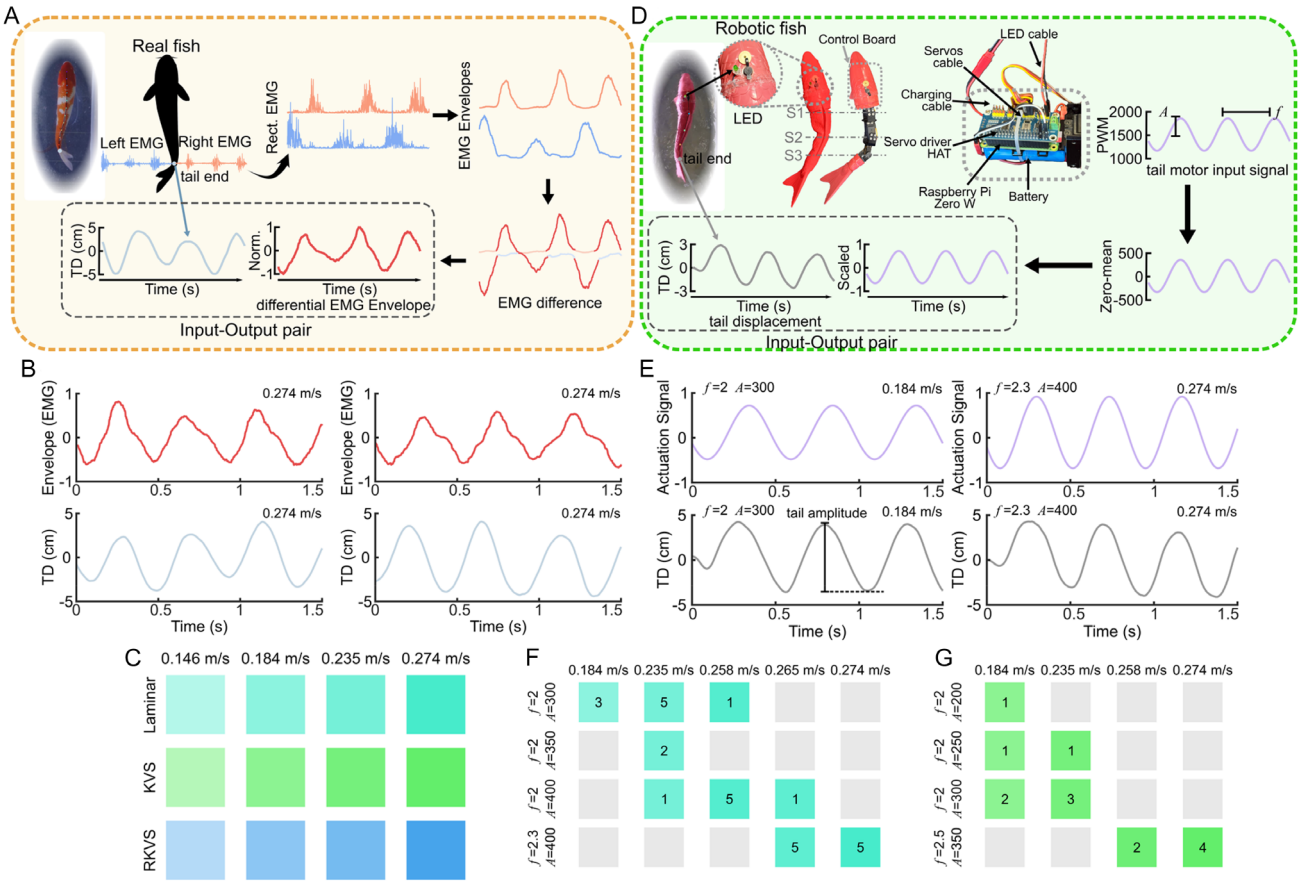

Figure 2. A) Real-fish signal processing pipeline for generating input–output pairs for the ARX model. Raw EMG filtered, rectified, and smoothed to extract envelopes. Left–right difference computed to form a single differential EMG signal. Normalized differential EMG used as ARX input and corresponding TD as model output. B) Examples of input–output pairs and flow conditions from real-fish experiments. C) Matrix of experimental conditions representing the full set of collected datasets. D) Signal processing pipeline for generating input–output pairs from the robotic fish for ARX model validation. Robotic fish actuated by three servos in a flexible body under open-loop CPG control. PWM signal from tail servo (S3) zero-mean corrected and normalized. TD from video used as model output. E) Representative input–output pairs from the robotic fish and matrix of flow speeds, and CPG parameters for robotic-fish experiments F) laminar flow (28 datasets) and G) KVS (14 datasets). The numbers in each colored tile indicate the datasets collected for that condition.

reasonably high R^2 values across multiple target datasets, suggesting that simpler flow regimes may promote better generalization. In contrast, RKVS-trained models (e.g., ARX_2 and ARX_4) showed limited generalization, often yielding low or negative R^2 scores when applied to datasets collected under different vortex conditions, indicating negative transfer.

Overall, this cross-validation matrix provides a rigorous means of evaluating model robustness across individual variability and flow environments. It highlights both the strengths and limitations of linear SySID methods like ARX in capturing the diversity of biologically generated locomotion signals.

2.2. Generalization Analysis via Residuals

While cross-validation using R^2 values captures overall prediction accuracy, it does not reveal detailed error structures or whether predictive failures arise from systematic model bias or unmodeled dynamics. To address this, we performed a residual-based generalization analysis using a representative ARX model trained on Dataset 1 (ARX_1). The goal was to assess whether prediction errors (residuals) exhibited temporal correlation or input dependence when applied to both self and unseen datasets.

For each test case, residuals $e_t = y_t - \hat{y}_t$ were analyzed using i) autocorrelation of the residuals and ii) cross-correlation between the model input and residuals. These metrics help evaluate whether residuals approximate white noise (ideal case) or contain structure suggestive of missing dynamics.

Figure 3F shows the residual analysis for the self-validation case (Dataset 1 → Dataset 1), where both autocorrelation and cross-correlation plots indicate minimal temporal or input-linked structure. This confirms that ARX_1 captures the majority of system behavior in its own training dataset, which was collected under laminar flow. In contrast, when ARX_1 was applied to Dataset 4 (Figure 3G), which was recorded under a RKVS condition, residuals exhibited temporal autocorrelation and stronger input-residual cross-correlation. These structured errors likely reflect flow-regime mismatch, as the ARX model trained in laminar flow cannot fully account for unsteady external perturbations

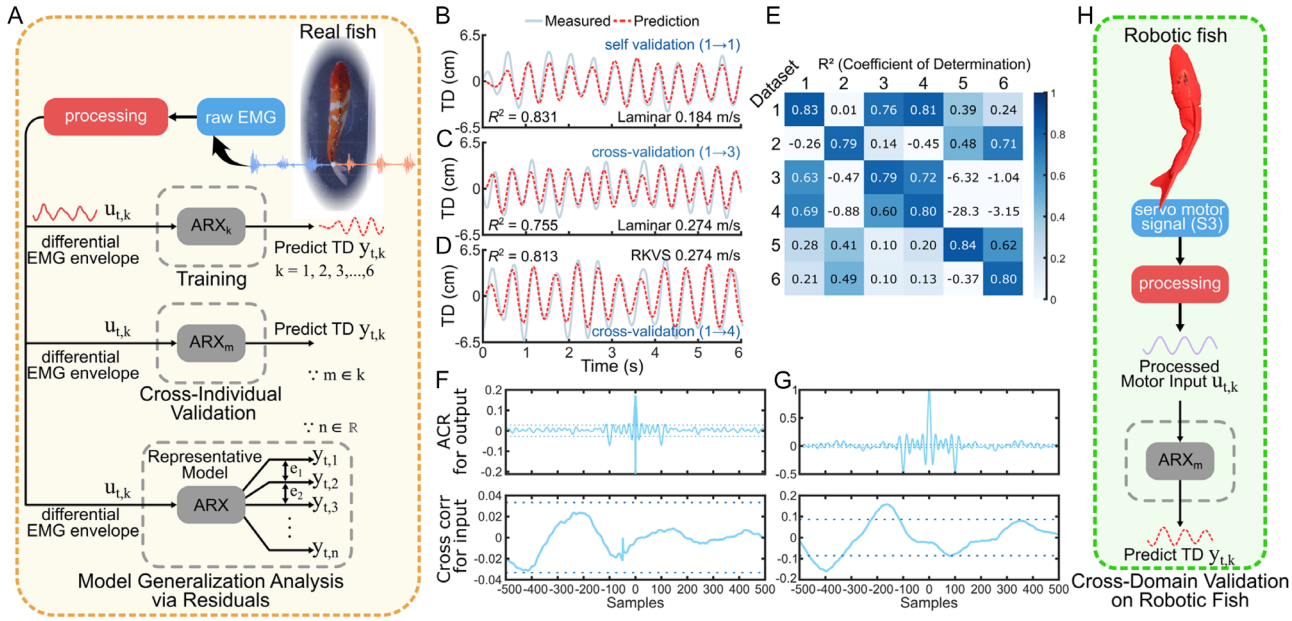

Figure 3. Workflow of ARX model training and validation. A) Six models trained on differential EMG–TD datasets from real fish and evaluated across all datasets to assess cross-individual generalization. B–D) Measured (gray) versus predicted (red dashed) TD for self- and cross-validation cases. E) R^2 cross-validation matrix. F,G) Residual autocorrelation and input–residual cross-correlation for (F) self and (G) cross cases. H) Cross-domain validation: ARX trained on biological data employed to predict robotic-fish TD from processed servo signals.

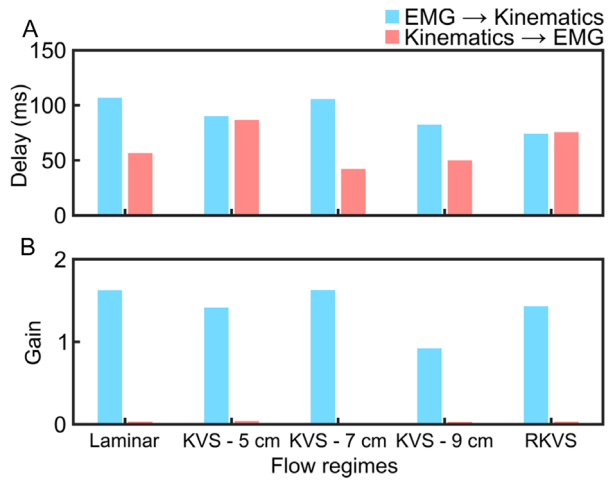

Figure 4. Delays and gains of ARX models mapping between EMG and tail kinematics across different flow regimes. A) Input–output delay (ms) and B) steady-state gain were extracted from ARX (3,3,n_k) models trained in the feedforward (EMG → Kinematics, blue) and feedback (Kinematics → EMG, red) directions. The optimal input delay n_k was selected for each model by sweeping n_k from 0 to 300 ms and choosing the value that maximized the PFI. Each bar represents the mean across multiple trials of fish ($N = 3$) tested under five distinct hydrodynamic conditions (laminar, KVS: 5, 7, 9 cm, and RKVS) at four swimming speeds (0.146, 0.184, 0.235, and 0.274 m s^{-1}).

introduced by vortex shedding in RKVS. Together, these results support the interpretation that generalization limitations of ARX models may arise from both biological variability and changes in environmental flow conditions.

2.3. Interpretation of System Behavior

To further characterize the sensorimotor system's dynamic behavior, we performed a pole-to-parameter transformation using the second-order approximation of a reduced-order ARX (2230) model. Although the primary modeling and residual analysis were conducted using the higher-order ARX (3330) model, both configurations yielded comparable fit indices and cross-individual generalization performance. Moreover, the pole-zero structures observed across both models were consistent, supporting the validity of this approximation. The continuous-time transfer function derived from ARX (2230) exhibited a natural frequency of $\omega_n = 11.3 rad/s$, indicating the dominant oscillation rate of the fish body in response to normalized unit EMG input. The system exhibited a low damping ratio $\zeta = 0.096$, suggesting that tail motion is underdamped and characterized by resonant, oscillatory behavior—a hallmark of compliant axial structures in undulatory swimmers. Based on these parameters, the settling time of the system was estimated as $T_s \approx 3.66$ s, capturing the time required for the tail to stabilize after a perturbation.

Additionally, the input–output delay T_d was extracted from the exponential term in the continuous-time transfer function derived from the fitted ARX model. In the Laplace domain, a pure time delay of T_d seconds is represented as a multiplicative factor e^{-sT_d} applied to the system's transfer function $G(s)$.[35] In our case, the identified transfer function included a delay term $e^{-0.029s}$, indicating a time delay of $T_d = 29$ ms. This formulation aligns with standard system modeling principles, in which the Laplace variable s has units of inverse time and the exponent remains dimensionless. The presence of this delay captures the combined effects of neural transmission latency and the

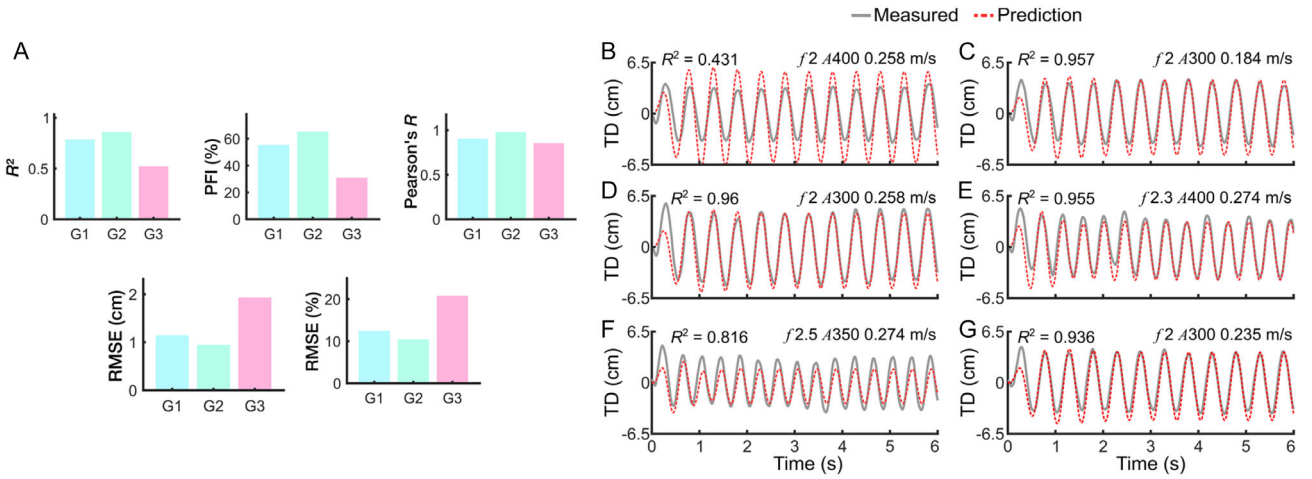

Figure 5. A) Summary of ARX prediction performance across the three real-to-robot standard-length ratio groups: G1 (≈1.04), G2 (≈0.8), and G3 (≈0.6). Bars show mean values of key metrics—R^2, PFI, Pearson's R, RMSE (cm), and normalized RMSE (%). Representative ARX model predictions for robotic-fish TD. B–E) Comparison of measured (gray) and ARX-predicted (red dashed) TD under different flow speeds and CPG control settings in laminar flow. F,G) Corresponding comparisons under KVS flow. Examples illustrate both high-accuracy cases and one lower-accuracy case at high actuation amplitude for laminar and KVS flow conditions.

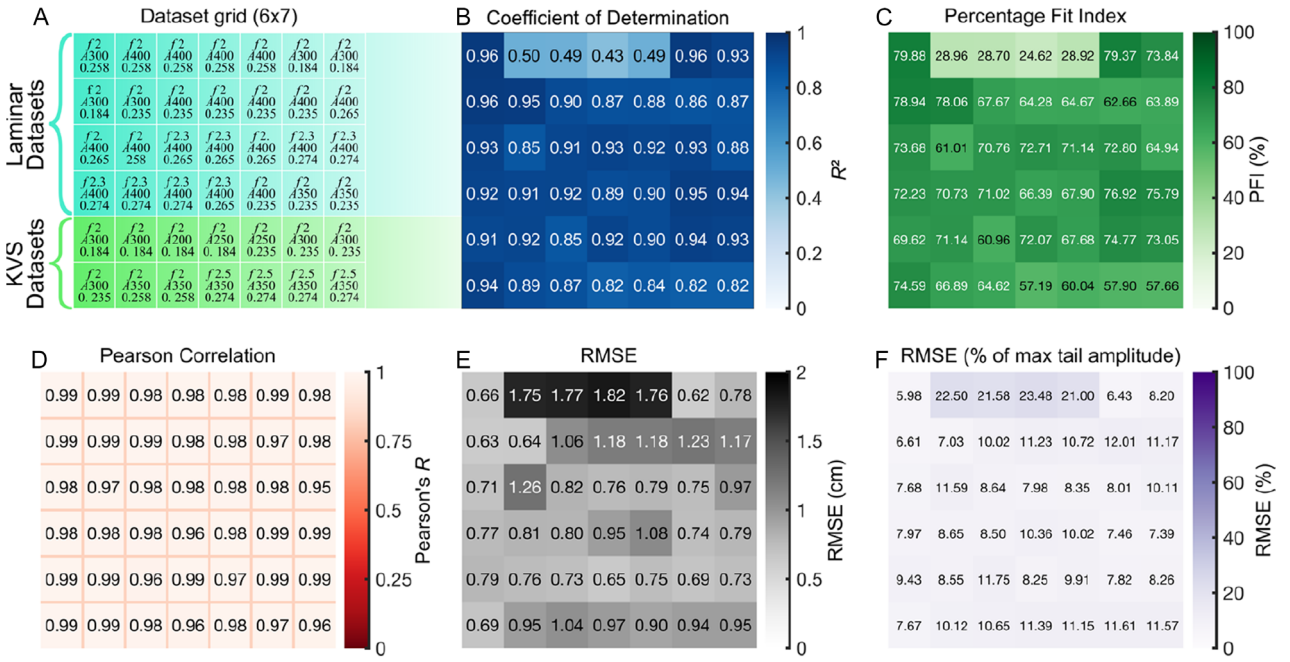

Figure 6. Validation metrics for robotic-fish datasets used to evaluate ARX model predictions. A) Experimental conditions for robotic-fish datasets (laminar: row 1 to 4 and KVS: row 5 to 6) used in ARX model validation. Each cell lists the CPG control parameters (frequency f and amplitude A) and the flow speed (m s^{-1}). B) R^2 between predicted and measured TD. C) PFI (%), indicating relative prediction accuracy. D) Pearson correlation coefficient R, reflecting the linear similarity between predicted and measured TD signals. RMSE of ARX model predictions across robotic-fish datasets, evaluated in two complementary forms. E) RMSE values in centimeters quantify the absolute prediction error in TD. F) RMSE is expressed as a percentage of the maximum TD amplitude for each dataset, providing a normalized view of model performance and facilitating interpretation across variable motion scales.

muscle electromechanical response, enabling a biologically meaningful characterization of the sensorimotor pathway.[36–38] These parameters together support a dynamic characterization of the fish's body as a low-damped, resonant actuator with fast response properties and moderate compliance. Such features are advantageous for efficient thrust generation and energy transfer during continuous swimming.

Moreover, these dynamics provide a valuable reference for assessing interindividual variability and for benchmarking the design of biomimetic robotic counterparts. The second-order

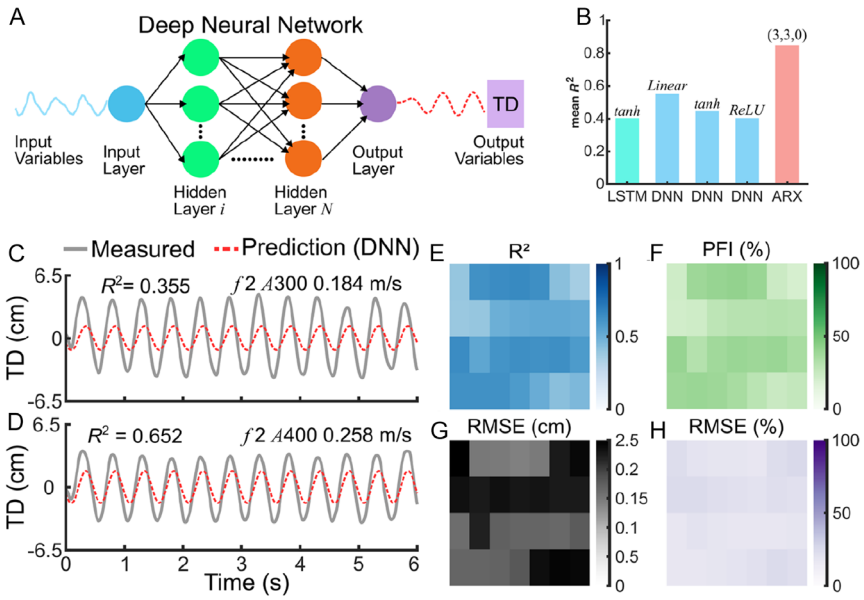

Figure 7. Cross-domain validation of a DNN trained on G2 fish EMG and kinematics, and tested on laminar flow datasets of robotic-fish motor signals to predict TD. A) Schematic of the DNN architecture. B) Comparison of mean R^2 across optimized deep-learning architectures, including DNNs with Linear, tanh, and ReLU activation functions, and an LSTM network, benchmarked against the ARX(3,3,0) model. C,D) Comparisons of measured (gray) and the optimized DNN (linear) predicted (red) TD for two representative robotic-fish datasets with the (C) lowest and (D) highest prediction accuracy. E–H) Performance of the optimized DNN across robotic-fish laminar flow condition (28 datasets): (E) R^2, (F) PFI, (G) RMSE, and (H) normalized RMSE (%).

Table 1. Datasets (G2) used for ARX model training and cross-individual validation, showing flow regime and flow speed for each dataset.

Dataset	Flow regime	Flow speed [m s^{-1}]
1	Laminar	0.184
2	RKVS	0.274
3	Laminar	0.274
4	RKVS	0.274
5	Laminar	0.274
6	Laminar	0.184

dynamics identified from our fish locomotion model, with a natural frequency $\omega_n = 11.3\text{rad/s}$ and a damping ratio $\zeta = 0.096$, suggesting that the fish body behaves as a lightly damped resonant system. This implies that the fish's tail reaches peak displacement approximately every $T = 2\pi/\omega_n \approx 0.556\text{s}$, setting a benchmark for tail-beat timing in robotic design. The corresponding settling time $T_s = 4/\zeta\omega_n \approx 3.66\text{s}$ defines the system's full-body stabilization window, which must be accounted for when designing feedback or adaptation in robotic motion. The gain of the system (≈25–30 from our transfer function) indicates that small-amplitude EMG signals result in relatively large mechanical responses, guiding actuator selection toward high-displacement response per unit input voltage or PWM duty cycle. Most critically, the identified input–output delay $T_d = 29\text{ms}$ sets a lower bound for real-time control loop latency in the robotic platform. This necessitates low-latency motor drivers and real-time processing (e.g., update rates above ≈35 Hz) to match the biological system's responsiveness. Together, these parameters allow the robotic fish to be tuned not just for kinematic resemblance, but also for dynamic equivalence, ensuring that the body oscillations, timing, and energy efficiency mirror those of the biological template.

2.4. Interpretability of ARX Model Parameters Reveals Sensorimotor System Dynamics

Beyond system behavior, ARX models offer mechanistic insights into the biological system through interpretable parameters such as input–output delay and steady-state gain. Figure 4 illustrates these parameters extracted from ARX (3, 3, n_k) models fitted in two directions: feedforward (EMG → kinematics) and feedback (kinematics → EMG), across hydrodynamic flow speeds and regimes. Figure 4A shows that feedforward models exhibited consistently longer delays (85–110 ms) than feedback models (45–80 ms), consistent with expectations of longer neuromuscular processing latencies relative to sensory feedback loops. Figure 4B highlights that the steady-state gain—indicative of how much motion is produced per unit of EMG input—was markedly higher in the EMG → kinematics pathway, suggesting a strong forward drive from muscle activation to body displacement. This asymmetry between the two pathways reflects canonical features of biological motor control: slower, high-gain forward transformation (muscle-driven motion) and faster, low-gain feedback transformation (sensory responsiveness). Such physiologically meaningful distinctions cannot be directly inferred from the latent weights of DNNs, which, while powerful for prediction at high computation cost and extensive data, lack transparency in revealing underlying system properties. The ability of ARX models to capture and quantify such delays and gains underscores their utility not only as predictive tools but also as

computational probes into the sensorimotor architecture of swimming fish.

2.5. Cross-Domain Generalization from Biological to Robotic

2.5.1. Influence of Real-to-Robot Size Ratio on Transfer Performance

To examine how morphological scaling between real and robotic fish affects cross-domain model performance, the experimental subjects were grouped according to their real-to-robot standard-length ratio. Three representative groups were defined: G1 (≈1.04), corresponding to fish closely matched to the robotic fish size; G2 (≈0.8), representing moderately smaller fish; and G3 (≈0.6), representing the smallest relative individuals (Table 4). From each group, multiple datasets were selected, and independent ARX models were trained using the corresponding EMG–kinematics pairs (Figure S4, Supporting Information).

The best-performing ARX model from each group was then evaluated on 42 robotic-fish datasets (Figure 6A) to quantify the effect of size ratio on cross-domain predictive accuracy. Figure 5A summarizes the results across five complementary metrics: R^2, PFI (%), Pearson's R, RMSE (cm), and normalized RMSE (%).

Performance analysis revealed a clear dependence of transfer accuracy on body-size similarity between biological and robotic systems. Groups G1 and G2, whose size ratios were closer to unity, achieved substantially higher prediction accuracy and lower error compared to G3, indicating that geometric and hydrodynamic similarity facilitates more faithful transfer of actuation–response dynamics. Among these, G2 exhibited the overall best performance, with the highest mean R^2 and PFI values and the lowest RMSE. The ARX model trained on G2 data was therefore selected as the representative biotrained model for all subsequent cross-domain validation experiments.

These findings highlight that while the proposed ARX framework generalizes across morphological variations, maintaining a comparable real-to-robot body ratio strengthens the fidelity of dynamic correspondence and improves prediction robustness.

2.5.2. Model's Prediction Performance for Cross-Domain Prediction

Representative ARX model predictions for robotic-fish TD across different flow regimes, speeds, and actuation parameters are presented in Figure 5B–G. The ARX model, which was exclusively trained on G2 fish EMG and corresponding kinematic data, was then validated by processed PWM as input, demonstrating robust performance in predicting robotic-fish TD, despite significant differences in system mechanics and actuation modalities.

Predictions shown in Figure 5C–G illustrate excellent agreement between predicted and measured TD, with coefficient of determination (R^2) values consistently exceeding 0.8 in laminar (Figure 5C–E) and KVS (Figure 5F,G) flow conditions. This indicates the ARX model effectively captured fundamental underlying dynamics transferable from biological locomotion to a bioinspired robotic system. However, Figure 5B illustrates a less accurate prediction ($R^2 = 0.431$) in the laminar flow regime, highlighting conditions under which the model exhibited reduced performance. This discrepancy was observed under high actuation amplitude conditions, suggesting potential nonlinearities or unmodeled dynamics in the robotic fish's response at these settings (Figure S6, Supporting Information). This drop-in accuracy may reflect either input–output mismatch (e.g., due to atypical CPG amplitude/frequency combinations) or dynamic features specific to the robotic platform (such as inertial lag or nonlinear actuator–fluid coupling) that were not captured by the linear model trained on biological data (Figure S5, Supporting Information).

Comparatively, previous studies employing CPG-driven robotic platforms to mimic fish or salamander locomotion typically focus on replicating general locomotion patterns rather than precisely predicting trajectories from biological data.[39] In contrast, our work provides explicit evidence that linear parametric models trained using real biological signals can accurately predict detailed kinematic outputs in robotic counterparts. The success of the ARX in this domain-shift stems from its parametric structure: it models the essential temporal and amplitude relationships between actuation and movement, rather than relying on complex, data-hungry patterns. Because these relationships (e.g., delay between actuation and motion, proportional gain, and oscillatory frequency) are shared by both fish and robots, the ARX can operate effectively in both worlds. This makes it more robust than high-capacity black-box models when facing the large gap between biological and robotic systems. These examples underscore the model's ability to generalize across domains while highlighting the need for further refinement or nonlinear modeling approaches in certain edge cases. A complete quantitative assessment across all robotic conditions is provided in Figure 6B–F.

To systematically evaluate prediction accuracy across all robotic datasets, several quantitative metrics were computed: the coefficient of determination (R^2), PFI, Pearson correlation coefficient (R), and RMSE. These metrics capture prediction accuracy from both absolute and normalized perspectives.

As detailed in Figure 6B–F, the ARX model exhibited high average predictive accuracy across 42 distinct robotic datasets (Figure 6A), yielding a mean R^2 of 0.86 ± 0.13, PFI of $65.25\% \pm 13.52$, and Pearson's R of 0.98 ± 0.008. The corresponding RMSE, shown in Figure 6E,F, averaged 0.95 ± 0.32 cm, which corresponds to roughly $10.44\% \pm 4.13\%$ of maximum TD amplitude, indicating consistently low prediction errors.

These results illustrate that the linear ARX model's performance remains stable despite significant variations in robotic operating conditions, highlighting the strength of parametric linear models for generalization to related but distinct mechanical systems. Prior works using similar approaches have typically emphasized domain-specific predictions or required extensive parameter tuning, and have rarely demonstrated robust generalization between biological and mechanical systems.[32] Thus, our study fills a notable gap by demonstrating robust predictive generalization from real biological measurements to robotic-fish dynamics.

2.6. Comparison of ARX and DNN Model Generalization to Robotic Fish

2.6.1. DNN Performance on Robotic Datasets

To benchmark against the linear ARX model, we implemented two machine learning (ML) models—a fully connected feedforward

DNN and long short-term memory (LSTM)—for predicting TD from EMG-derived inputs.[40] We trained the ML models using six G2 fish datasets (Table 1). To ensure a fair and optimized comparison with the ARX model, the feedforward DNN was retrained under multiple configurations with systematic optimization of activation functions, regularization, and training callbacks. The DNN architecture consisted of sequential layers with [1, 128, 64, 32, 16, dropout (0.2), 1] neurons (Figure 7A). Three activation settings were evaluated: i) linear activations in all layers, ii) tanh activations in hidden layers with a linear output, and iii) ReLU activations in hidden layers with a linear output. We used a linear activation function at the output layer for all networks because the data were not normalized, and the TD values were retained in their original physical scale and units. The network was trained using the Adam optimizer (learning rate 1×10^{-4}), mean squared error loss, and RMSE as the training metric. Early stopping (patience = 3) and adaptive learning-rate scheduling (ReduceLROnPlateau, factor = 0.5, patience = 5, minimum learning rate = 1×10^{-6}) were applied to prevent overfitting and stabilize convergence. Training was performed for up to 1000 epochs, with a batch size of 300 and a 30% validation split.

Similarly, the LSTM network was implemented to represent a state-of-the-art nonlinear time-series baseline. For this model, the input–output data were converted to a sequential form using a sliding-window method. A window length of 4 was used, producing overlapping sequences that transformed the original input matrix of size (n, m) into a 3d array ($n-4+1$, 4, m), where each window captured four consecutive time steps of the input variables aligned with their corresponding output values. The LSTM architecture comprised stacked layers [64, 64, 64, 32, 16] with a 20% dropout and a linear output layer, trained under the same optimization settings and callbacks as the DNN.

Model performance was quantified using the coefficient of determination (R^2) on the cross-domain (bio-to-robot) test set. Figure 7B shows the resulting mean R^2 values were 55.16% (DNN-linear), 44.15% (DNN-tanh), 43.39% (DNN-ReLU), and 40.42% (LSTM). We selected the optimized DNN with a linear activation function among all the ML models due to its relatively better predictive performance.

Representative robotic-fish trials illustrate the variability in DNN performance (Figure 7C,D). In one case (flow speed = $0.258\,\mathrm{m\,s^{-1}}$, $f = 2$, $A = 400$), the model achieved $R^2 = 0.652$, indicating moderate accuracy (Figure 7C). In contrast, under different conditions ($0.184\,\mathrm{m\,s^{-1}}$, $f = 2$, $A = 300$), performance dropped sharply to $R^2 = 0.355$ (Figure 7C). Across all robotic datasets, the DNN achieved a mean R^2 of 0.55 ± 0.096, RMSE of 1.987 ± 0.368 cm, PFI of $32.74 \pm 6.95\%$, and normalized RMSE of $20.50 \pm 2.63\%$; their distributions are shown in Figure 7E–H.

The DNN exhibited lower predictive accuracy and higher average error than the ARX model, despite being trained on more biologically relevant datasets. This finding aligns with previous literature showing that deep models, although powerful in representation capacity, are often more sensitive to domain shifts and less robust to limited training diversity without additional adaptation techniques.[32]

2.6.2. Quantitative Comparison with ARX Model

Table 2 summarizes the performance of ARX and DNN models, both trained on real-fish datasets and validated on robotic-fish data (laminar flow condition). Across all metrics, the ARX model consistently outperformed the DNN: 1) Coefficient of determination (R^2): 0.85 ± 0.15 versus 0.55 ± 0.096 (+56.5% improvement); 2) PFI: $64.73 \pm 16.22\%$ versus $32.74 \pm 6.95\%$ (+97.8% improvement); 3) Pearson's R: 0.98 ± 0.008 versus 0.90 ± 0.053 (+8.9% improvement); 4) RMSE: 1.08 ± 0.372 cm versus 1.987 ± 0.368 cm (54.35% error reduction); and 5) normalized RMSE: $10.73 \pm 5.02\%$ versus $20.50 \pm 2.63\%$ (47.6% error reduction).

These results demonstrate that, for cross-domain prediction from limited biologically derived datasets, the ARX model delivers substantially higher predictive accuracy and lower error than the DNN. The parametric structure and modest data requirements of ARX models facilitate robust generalization across biological and robotic domains. While prior work has often favored deep learning for bioinspired robotics due to its representational flexibility,[32] our findings show that simpler, interpretable models can achieve superior performance under realistic bio-to-robot transfer scenarios. In the context of cross-domain transfer, this is particularly important: a model that works well without retraining enables us to leverage insights from real animal data and deploy them directly in bioinspired robots, even when their mechanics differ substantially. This removes the need for costly robot-specific data collection and opens the door to building robotic systems grounded in actual biological function rather than mere imitation. Beyond accuracy, ARX models provide physiologically meaningful parameters, such as delays and gains, giving us direct insight into the underlying sensorimotor architecture of real fish; such capabilities are inherently lacking in black-box models like DNNs.

2.6.3. ARX Versus Deep Models: Complexity and Computational Trade-Offs

Beyond predictive accuracy, the ARX and DNN frameworks differ substantially in their computation, data requirements, deployment, and interpretability (**Table 3**). The ARX (3,3,30) model comprises only six coefficients plus a bias term, can be fitted in closed form on a CPU within milliseconds, and operates with microsecond-level latency per prediction step—making it

Table 2. Quantitative comparison of ARX and DNN performance on robotic-fish validation datasets. Metrics are reported as mean ± SD across 28 datasets. The last column shows the relative performance of ARX versus DNN.

Validation metrics	ARX (Mean ± Std)	DNN (Mean ± Std)	Relative performance (ARX/DNN)
R^2	0.85 ± 0.15	0.543 ± 0.096	+56.5%
PFI (%)	64.73 ± 16.22	32.74 ± 6.95	+97.8%
Pearson's R	0.98 ± 0.008	0.9 ± 0.053	+8.9%
RMSE [cm]	1.08 ± 0.37	1.987 ± 0.368	−54.35% (error reduction)
Normalized RMSE	10.73 ± 5.02	20.50 ± 2.63	−47.6% (error reduction)

Table 3. Practical comparison of ARX, DNN, and LSTM (this study).

Aspects	ARX(3,3,30)	DNN (Linear)	LSTM
Parameters	6 (+bias)	11137	98513
Model memory (float32)	≈28–32 bytes	≈44 kB	384
Saved model size	7 KB	290 kb	4.5 MB
Training hardware	CPU	GPU recommended	GPU recommended
Typical train time (fish data)	ms	minutes (with tuning)	minutes (with tuning)
Inference per time step	≈10 ops	$\approx 2.4 \times 10^4$ ops	$\approx 3.8 \times 10^5$ ops
Time per inference step	µs	1 ms	6 ms
Data needs	Low	High	High
Zero-shot fish to robot	Yes	weak (domain-shift sensitive)	weak (domain-shift sensitive)
Interpretability	High (delays/gains/damping)	Low	Low
Ability to capture nonlinearity	Limited (linear only)	Strong (via nonlinear activations)	Very strong (temporal + nonlinear)

Table 4. Subject information for freely swimming real-fish experiments, showing weight and standard length of each fish.

Fish group (Ratio)	Subject	Weight [kg]	Standard length [cm]	Mean standard length [cm]
G1 (≈1.042)	1	0.915	32	34.4 ± 1.51
	2	0.960	34	
	3	1.160	35	
	4	1.160	35	
	5	1.070	36	
G2 (≈0.8)	1	0.50	26	26.5 ± 0.9
	2	0.46	25.5	
	3	0.53	27.5	
	4	0.56	27	
G3 (≈0.6)	1	0.25	20	19.62 ± 1.8
	2	0.2	17	
	3	0.25	20.5	
	4	0.28	21	

well-suited for real-time or embedded applications. In contrast, the DNN used here contains 11 137 trainable parameters, requires GPU-accelerated training with hyperparameter tuning, and performs approximately O (10^4) multiply–accumulate operations per time step during inference.

The ARX model is data-efficient, transferring from fish to robot in a zero-shot manner without retraining, whereas the DNN exhibited greater sensitivity to domain shift between biological and robotic systems. Moreover, ARX models are inherently interpretable: key parameters such as delay, steady-state gain, and damping ratio can be directly extracted, providing mechanistic insight into the underlying sensorimotor system.

DNNs and LSTMs, by contrast, offer greater nonlinear representational capacity and can capture richer temporal dependencies when large, diverse datasets are available. However, they trade off interpretability and computational simplicity for complexity and hardware demands.

Overall, for cross-domain prediction tasks involving limited biological data, the compact ARX model achieves higher efficiency and interpretability at a fraction of the computational cost, while maintaining robust accuracy. Deep learning architectures remain advantageous primarily when strong nonlinearities dominate and extensive domain-specific data are accessible.

3. Conclusion

This study presented a biologically grounded cross-domain modeling framework that captures the sensorimotor dynamics of freely swimming koi fish and evaluates their offline transferability to a robotic fish without retraining. Our primary objectives were to 1) develop an interpretable SySID-based plant model capable of generalizing beyond its training conditions, 2) quantify bidirectional EMG $\leftrightarrow$ kinematics relationships to extract dynamics-relevant parameters, and 3) assess robustness to variability in individual fish, morphology, and operating environment. Objective 1 was achieved by training an ARX model on real-fish datasets collected across four hydrodynamic regimes and multiple swimming speeds (0.146–0.274 m s^{-1}), followed by offline testing in which the selected fish-trained ARX model received processed PWM actuation signals from a robotic fish and predicted its TD. Objective 2 was met by extracting parameters such as natural frequency, damping ratio, input–output delay, and steady-state gain, revealing pathway-specific differences consistent with biological motor control principles. Objective 3 was ticked off by cross-individual and cross-domain evaluations, where the ARX model outperformed the DNN baseline with a 56.5% higher R^2, 97.8% higher PFI, and up to 54.35% lower RMSE in robotic-fish predictions, demonstrating resilience to biological and mechanical differences. These results demonstrate that interpretable, low-fidelity SySID models can capture biologically meaningful motion dynamics and apply them effectively across domains in an offline predictive setting, even under significant physical and environmental differences. Beyond robotics, the extracted parameters provide new physiological insight into fish sensorimotor loops and offer a practical basis for tuning bioinspired controllers. Future work will address

the observed performance drop under high-amplitude actuation, potentially through nonlinear or hybrid ARX–nonlinear approaches or polynomial state-space formulations. Additional directions include extending the framework to multi-degree of freedom morphologies, integrating closed-loop sensory feedback for adaptive control in unsteady flows, and validating across diverse species and robotic platforms.

4. Experimental Section

Animal Care and Housing: All experimental procedures and animal handling were approved by the Institutional Animal Care and Use Committee of Peking University (Certificate No. TY2018466).

Carp fish (*Cyprinus rubrofuscus* and *Cyprinus carpio*) were obtained from a local fish market for experimental use (see **Table 4**). The fish were categorized into three groups based on the ratio of real-fish to robotic-fish standard length, calculated as the mean standard length of each real-fish group divided by the standard length of the robotic fish. The animals were housed in a well-maintained $2 \times 4 \times 0.3\ m^3$ tank with a total volume of 2400 liters. Water quality was maintained by replacing one-third of the volume weekly with fresh, dechlorinated water and through continuous filtration at a rate of $6000\ L\ h^{-1}$. Water temperature was kept at $20 \pm 2\ °C$.

Fish were fed three times daily using an automated feeding system. Following the completion of all experimental procedures, the fish were returned to a communal lake environment to reintegrate with other conspecifics.

EMG Electrode Implantation and Recording System: Fish were first anesthetized using a $160\ mg\ L^{-1}$ solution of tricaine methanesulfonate (MS-222), continuously circulated through the mouth and gills to maintain anesthesia during electrode placement. While under anesthesia, the fish's weight and standard length were measured, and electrode implantation sites were marked near the base of the caudal fin (caudal peduncle) on both sides of the body.

Differential EMG signals were recorded bilaterally by implanting electrodes in the red muscle using fine (0.1 mm diameter), insulated copper wires with 10 mm of insulation stripped from both ends. Each wire was inserted through a 28-gauge hypodermic needle and bent into a hook shape to remain embedded in the muscle after needle withdrawal. Electrodes were placed symmetrically on the left and right sides near the caudal peduncle, while a reference electrode was positioned near the left gill, away from the differential pairs.

The recording system (Figure 1D) comprised a wireless 16-channel differential biosignal acquisition device (FreeBCI-BT-16, Nanjing Chengpu Electronic Technology Co., Ltd.), which integrates signal amplification, analog-to-digital conversion, and on-board microSD storage. The device supported remote operation and enabled untethered, high-fidelity EMG recordings during free-swimming trials.

To improve signal stability and reduce drag-induced dislodgement, electrodes were sutured to a dorsal fin ray and glued together, leaving just enough slack to accommodate full-body undulations without detachment. This design minimized motion artifacts, reduced water resistance, and eliminated tangling. The protocol was refined through trial and error, allowing us to reduce experimental preparation times from several months to a few weeks.

Following electrode placement, fish were transferred to the water treadmill (Loligo; Figure 1B) for recovery in home tank water. After 30 min of recovery, EMG recordings were initiated during steady swimming across four flow speeds: 0.146, 0.184, 0.235, and $0.274\ m\ s^{-1}$. Concurrently, a high-speed camera (Sony RX100m5) mounted above the tunnel captured top-view videos at 100 fps to extract body midline and TD data (Figure 1A, see Figure S1, Supporting Information).

Experimental Protocols and Flow Conditions: Experiments were conducted under three distinct flow regimes: laminar flow, KVS, and RKVS, as illustrated in Figure 1E–G. (for details Movie S1, Supporting Information) Kármán vortices were generated using D-section cylinders (5, 7, 9 cm), following established vortex generation protocols.[41] Reverse Kármán vortices were created by actuating a 3D-printed caudal fin at 1.5 Hz. The fin was fabricated using Future TPU material (https://www.wenext.cn/static/material/78), which conforms to ISO 10993-10 and ISO 10993-5 standards for skin sensitivity and cytotoxicity.

All experiments were performed at four flow speeds: 0.146, 0.184, 0.235, and $0.274\ m\ s^{-1}$. We measured water velocity at the center of the test section using a turbine-type flow probe (LS300A) in the absence of the fish. To ensure consistency with the fish's natural environment, each subject was tested in the water treadmill filled with water from its home tank. Fish were first acclimated in laminar flow at $0.124\ m\ s^{-1}$ for 30 min. After acclimation, the flow speed was increased to the designated value, and the fish swam under laminar flow for 1 min before EMG and kinematic data were recorded for an additional 1–2 min (Figure 1E).

Following the laminar trials, the flow speed was reduced to $0.124\ m\ s^{-1}$, and a D-section cylinder was introduced into the tunnel to generate Kármán vortices (Figure 1F). Fish were given 5 min to adapt to the vortex environment before data collection resumed under turbulent flow conditions at the specified speeds. EMG and kinematic data were again recorded for 1–2 min per condition.

This procedure was repeated using the RKVS configuration (Figure 1G), in which vortex patterns were induced via the flapping 3D-printed fin. Collectively, these trials yielded a diverse dataset encompassing fish sensorimotor responses and tail kinematics across a range of flow speeds and vortex environments. This dataset forms the basis for understanding how swimming muscle activation and body motion adapt to changes in hydrodynamic conditions.

Signal Processing and Pose Extraction: EMG Preprocessing Pipeline: Raw EMG signals recorded (1 kHz) by the biosignal acquisition system often contained noise from transmission lines and motion artifacts. To address this, we developed a custom MATLAB script for offline signal processing, and the processing pipeline is shown in Figure 2A. Each channel underwent the following preprocessing steps: Detrending to remove linear drift, high-pass Butterworth filtering at 20 Hz to eliminate low-frequency motion artifacts, low-pass Butterworth filtering at 450 Hz to remove high-frequency noise, and Notch filtering at 50 Hz to suppress power line interference.

After filtering, signals were rectified (full-wave) to extract amplitude envelopes, followed by double-pass smoothing with a 50-sample moving-average filter. To generate a single input signal for single-input-single-output (SISO) ARX, the right EMG envelope was subtracted from the left, resulting in a differential EMG envelope. This signal was then normalized and used as the ARX model input, while the corresponding TD served as the model output.

Signal Processing and Pose Extraction: Video-Based Kinematic Extraction and Head-Frame Transformation (Real and Robotic Fish): We used DeepLabCut (DLC)[42] to extract midline poses from 100 fps video recordings of both real and robotic fish (Figure 1A–C). The DLC training dataset included 69 videos spanning various subjects and swimming speeds. In total, 1610 video frames were manually labeled with evenly spaced midline points from the eyes to the base of the caudal fin. The model was trained for 1×10^5 iterations using the Resnet-152 backbone under DLC's default settings.

A separate DLC model was trained for robotic fish, initialized from a ResNet-152 backbone and fine-tuned on manually annotated frames representative of their respective body shapes, colors, and backgrounds. For the robotic fish, equivalent points were selected to match the geometric configuration of its modular tail segments.

After inference, poses with likelihood scores above 0.9 were retained and visually verified by overlaying on the original video frames (Movie S1, Supporting Information). While the *x*-axis coordinates were stable, *y*-axis jitter was corrected using shape-preserving piecewise cubic interpolation (makima), which improved midline continuity.

To express body kinematics in a head-fixed coordinate system (essential for comparing real and robotic-fish data), we converted global DLC pose coordinates into joint angles and then reconstructed the pose using four body segments of equal length. The transformation was applied using the following homogeneous transformation matrix

$$ {}^{i-1}F_{t,i} = \begin{bmatrix} \cos\alpha_{t,i-1} & -\sin\alpha_{t,i-1} & 0 & P_{t,x,k,i} \\ \sin\alpha_{t,i-1} & \cos\alpha_{t,i-1} & 0 & P_{t,y,k,i} \\ 0 & 0 & 1 & 0 \\ 0 & 0 & 0 & 1 \end{bmatrix} \quad (1) $$

Here, $P_{t,x,k,i} = p_{t,x,k,i-1} - d_{t,x,i}$ and $P_{t,y,k,i} = p_{t,x,k,i-1} - d_{t,y,i}$ are the transformed midline points at time t and segment i. Angles $\alpha_{t,i-1}$ represent the orientation between segment $i-1$ and segment i. The terms $d_{t,x,i}$ and $d_{t,y,i}$ denote the x and y components of displacement between adjacent midline points p_{i-1} and p_i, respectively. These displacement vectors are used to transform each midline point p_k from the global coordinate frame into the head-attached coordinate frame (defined by $i = 1$), enabling consistent analysis of TD as shown in Figure 1A,C, Figure 2A,B, and Figure 2D,E.

Signal Processing and Pose Extraction: Generation of Synchronized Input–Output Pairs: Final input–output pairs consisted of synchronized differential EMG envelopes and head-relative TD trajectories. Synchronization was achieved using an light emitting diode (LED) pulse visible in both EMG and video recordings. Representative pairs are shown in Figure 2B for two trials at 0.274 m s^{-1}, demonstrating signal fidelity and interindividual variability. Figure 2C summarizes the complete dataset spanning various flow speeds and regimes.

Robotic-Fish Dataset Generation for Testing the Biosignal–Driven System Model: We used a custom-built, purposely modified robotic fish actuated by three serially connected servo motors (S1–S3) embedded within a flexible 3D-printed body (Figure 2D). The standard length of the robotic fish from nostril to caudal peduncle is 33 cm. The control unit—comprising a Raspberry Pi Zero W and a PWM Servo Driver HAT—executed an open-loop CPG to produce sine wave signals with constant phase lag between segments. The CPG parameters (frequency f, amplitude A) were selected based on the flow speed measured prior to each experiment. The system was powered by a rechargeable lithium battery connected via a switch, allowing easy start-stop control. Additional wiring enabled servo actuation, LED triggering for video synchronization, and recharging without disassembly.

Robotic-fish experiments were performed under laminar (Figure 2F) and KVS (5 cm cylinder) (Figure 2G) flow conditions. To calibrate actuation parameters for each flow speed, we used a turbine-type flow probe (LS300A) to measure the background flow. Actuation settings were tuned such that the fish could hold position without drifting, and then trials were recorded for 30 s per condition. A head-mounted LED provided a visual marker synchronized with motor actuation (Figure 2D).

Although all three servos were actuated, only the PWM control signal to the third servo (S3), located at the tail end, was used as the model input. This signal most closely represents the wave peak and hence is analogous to the caudal EMG activity observed in real fish. The raw PWM signal, typically oscillating around 1500 µs, was zero-mean corrected and normalized by dividing by 550 to scale it to the range [–1, 1]. This value was determined through a sensitivity analysis (Note S1 and Figure S3, Supporting Information), which showed that normalization factors between 550–700 provided optimal amplitude alignment between ARX-predicted and measured TD. Because the ARX model is linear in input, this calibration influences only amplitude (R^2/RMSE) without affecting timing or shape. The same normalization factor (550) was consistently applied across all real-fish size groups and robotic datasets. This preprocessing was intentionally designed to parallel the EMG preprocessing pipeline used for the real-fish data. We allowed the trained ARX model to treat PWM inputs as EMG envelopes by aligning the input signal characteristics, thereby preserving the learned mapping from actuation signal to TD. This equivalence in data format was critical for enabling direct bio-to-robot transfer. The corresponding TD measured from the video served as the model output (Figure 2).

Robotic-Fish Dataset Generation for Testing the Biosignal–Driven System Model: Generation of Synchronized Input–Output Pairs: Final input–output pairs consisted of the processed PWM input signal (from servo S3) and the corresponding TD in the head-attached frame. These were temporally aligned using the LED pulse visible in the video stream. Representative examples are shown in Figure 2E, highlighting trials conducted at 0.184 m s^{-1} ($f = 2$, $A = 300$) and 0.274 m s^{-1} ($f = 2.3$, $A = 400$). These signals were not used for model training but were reserved exclusively for validating the generalization performance of ARX models trained on real-fish EMG. The complete robotic dataset covered laminar and KVS flow regimes with 42 unique input–output conditions across flow speeds and multiple actuation settings. The number of trials for laminar and KVS flow regimes are shown in Figure 2F,G, respectively.

To ensure a comprehensive evaluation, the robotic datasets covered a wide range of actuation settings and environmental conditions. Figure 6A details the tested combinations of frequency–amplitude pairs and corresponding flow speeds used for each dataset. These datasets were organized in a 6×7 grid, with consistent indexing across the metric heatmaps shown in Figure 6A. Rows 1 to 4 of the grid represent laminar flow conditions trials, while rows 5 to 6 represent KVS flow condition trials.

Time-Series Modeling, Training, and Validation Workflow: To model the mapping from muscle activity to body kinematics in a swimming fish, we employed a linear ARX model (Figure 3A). The ARX framework offers several advantages that align with our goals of biological interpretability and robotic transfer. First, its structure explicitly captures time-domain relationships, making it well-suited for sequential motor behaviors.[22] This contrasts with frequency-domain or purely statistical models, which may obscure transient dynamics critical for swimming motion. Second, ARX models are computationally efficient and interpretable: each coefficient reflects a clear temporal contribution of past inputs or outputs, allowing direct physiological insights into muscle–motion coupling.[43] Additionally, the model's ability to incorporate fixed input–output delays enables alignment with known neuromuscular latencies, thereby facilitating biologically meaningful parameters.[37] The ARX framework is also one of the most extensively studied SySID methods, with demonstrated success in underwater robotics applications, including heave dynamics modeling,[44] yaw control optimization,[45] and dynamic modeling of marine vehicles under hydrodynamic disturbances.[46] This prior use in aquatic environments[44–49] means that ARX-estimated parameters such as natural frequency, damping ratio, and delay have direct physical relevance for aquatic vehicles, strengthening the credibility of transferring fish-trained models to robotic platforms. Its stability, maturity, and modest data requirements make it a reliable benchmark for evaluating more complex or nonlinear alternatives. Importantly, its simplicity and linearity support cross-domain generalization, which is essential for transferring models trained on biological data to robotic systems with similar kinematics but different actuation mechanisms. These features collectively make the ARX model an ideal candidate for building a model of the system that bridges biological and robotic domains.

The ARX model used in this study relates neuromuscular signals to kinematic outputs. Generally speaking, an ARX model[36] leverages delayed inputs and outputs to predict future output values over one or more sample intervals. The simplest form of the ARX model can be expressed as

$$ \hat{y}(t) = f(x(t)) \quad (2) $$

where $\hat{y}(t)$ corresponds to the model's predicted output, while $x(t)$ is a regression vector comprising current and past inputs, outputs, and prefiltered noise. The function $f(\cdot)$ defines the relationship between $x(t)$ and the prediction. For linear grey-box models, $f(\cdot)$ takes the form of a ratio of linear polynomials. A typical linear ARX model can be expressed as

$$ \begin{aligned} \hat{y}(t) + y(t)(a_1 q^{-1} + a_2 q^{-2} + \ldots + a_{n_a} q^{-n_a}) \\ = u(t - n_k)[(b_1 + b_2 q^{-1} + \ldots + b_{n_b} q^{-n_b+1})] + e(t) \end{aligned} \quad (3) $$

The model includes constant coefficients $a_1, a_2, \ldots, a_{n_a}$ and $b_1, b_2, \ldots, b_{n_b}$, which need to be estimated. Here, $\hat{y}(t)$ denotes the one-step-ahead prediction of the true output $y(t)$, and q^{-1} is the backward shift (or delay) operator. The input signal is represented by $u(t)$, and $e(t)$ denotes the additive noise. The term n_k specifies the number of delay steps (at least one), while n_a and n_b define the lengths of the output and input regression vectors, respectively (with n_b accounting for one additional term).

To apply the ARX framework to our problem, we constructed an independent SISO ARX model for fish TD. As mentioned in the previous section, the model was trained to map differential EMG input signals to TD, using synchronized datasets collected during free swimming. Our objective was to identify a model that not only fit the training data well but also generalized across different swimming trials and subjects.

An initial hyperparameter sweep was performed across multiple datasets to evaluate combinations of model orders n_a, n_b, and delay n_k. The parameters of the linear ARX models were identified using a conventional least-squares minimization approach, as described by.[43] We prioritized configurations that achieved high fitness to the measured output while maintaining model simplicity. A third-order model—denoted ARX (3, 3, nk)—emerged as a strong candidate due to its balance of performance and interpretability. This structure revealed two prominent poles across datasets (see Figure S2B, Supporting Information), which enabled further dynamic characterization of the system using second-order approximations (e.g., natural frequency ω_n and damping ratio ζ). The compact form also facilitated the interpretation of gain and temporal alignment between input and output signals.

The input–output delay n_k was determined through empirical testing. We systematically varied n_k and evaluated model performance across training and cross-dataset validation scenarios. The optimal delay was chosen such that the ARX model trained on one fish trial generalized well to other trials when provided with their EMG inputs, ensuring robustness across individuals. Ultimately, the ARX (3330) configuration was selected. This model consistently achieved high fit scores on both training data and unseen validation datasets, as seen in Figure 3B–E.

After estimating the model parameters, a more in-depth examination of the system's poles and gain was carried out to extract additional insights into its dynamics. Across trials, the fitted model exhibited two dominant complex-conjugate poles, suggesting the presence of a second-order sensorimotor mode in the fish body (see Figure S2, Supporting Information). Using standard pole-to-parameter transformations, we approximated key dynamic characteristics, including the natural frequency and damping ratio, which provide insight into the resonant behavior and compliance of the fish's axial system. This dynamic characterization complements the predictive function of the ARX model by offering interpretable metrics linked to the underlying biophysics. As such, the trained ARX (3330) model serves not only as a tool for mapping EMG to kinematics but also as a compact, interpretable representation of the fish's locomotor dynamics.

Once the model is trained on real-fish data, we evaluated its generalizability and practical utility by testing its ability to predict the kinematics of a robotic fish using processed servo signal as input (Figure 3H). This cross-domain deployment serves as a validation of the model's capability to transfer learned sensorimotor relationships from a biological system to a synthetic platform with similar morphological and dynamical characteristics. The robotic fish used in this study closely resembled the geometry and joint configuration of the real fish, with actuated tail segments mimicking the degrees of freedom captured in the kinematic data. The ARX (3330) model, trained solely on a single dataset of synchronized EMG and TD from a real swimming fish, was used in inference mode to predict robotic-fish TD from unseen PWM signals that drive the robotic-fish's servomotors in open-loop mode. The TD data for the robotic fish was obtained similarly to the real-fish data. Importantly, no robotic-fish data were used for training the ARX (3,3,30) model, as it was trained solely on biological EMG–TD pairs. For cross-domain testing, we ensured that the robotic-fish input signal (processed PWM) was preprocessed in the same way as the EMG, so the model would "see" an input in a familiar format. This careful signal conditioning made it possible for the ARX to interpret motor commands in the robotic fish as analogous to muscle activations in the real fish, enabling direct domain transfer without retraining.

It was observed during experimentation and verified by analysis (see Figure 3) that this cross-domain application requires no further retraining or tuning of the ARX model. Despite differences in material properties, actuation delays, and environmental interactions, the predicted TD trajectories elicited fluid and coordinated swimming motions in the robotic fish that qualitatively resembled those of the biological system. This result demonstrates that the ARX model successfully captured core sensorimotor dynamics transformations that are robust enough to be ported across domains. Furthermore, this evaluation highlights the value of compact, interpretable gray-box models in bioinspired robotics. The ability to map EMG-like actuation patterns into joint-level kinematics using a biologically informed SySID model offers a promising foundation for closed-loop control architectures and embodied neural interfacing in future soft robotic platforms.

Supporting Information

Supporting Information is available from the Wiley Online Library or from the author.

Acknowledgements

A.T. and R.H.A. contributed equally to this work. This work was supported in part by the National Natural Science Foundation of China under Grant U22A2062, Grant U23B2037, Grant 12272008, Grant W2442039, and Grant 61973007, and in part by the Beijing Natural Science Foundation under Grant 3242003. Furthermore, L.L. acknowledges funding support from the Max Planck Society, the Deutsche Forschungsgemeinschaft (DFG, German Research Foundation) under Germany's Excellence Strategy-EXC 2117–422037984, the Sino-German Centre in Beijing for generous funding of the Sino-German mobility grant M-0541, and Messmer Foundation Research Award.

Open Access funding enabled and organized by Projekt DEAL.

Conflict of Interest

The authors declare no conflict of interest.

Data Availability Statement

The data that support the findings of this study are available from the corresponding author upon reasonable request.

Keywords

bioinspired motion modeling, cross-domain generalization, electromyography, fish locomotion, robotic fish, system identification, time-series analysis

Received: September 12, 2025
Revised: November 3, 2025
Published online:

[1] K. H. Low, C. W. Chong, *Bioinspir. Biomim.* **2010**, *5*, 046002.
[2] G. V. Lauder, E. G. Drucker, *IEEE J. Oceanic Eng.* **2004**, *29*, 556.
[3] D. N. Beal, F. S. Hover, M. S. Triantafyllou, J. C. Liao, G. V. Lauder, *J. Fluid Mech.* **2006**, *549*, 385.
[4] Y. Li, Y. Xu, Z. Wu, L. Ma, M. Guo, Z. Li, Y. Li, *Int. J. Adv. Robot Syst.* **2022**, *19*, 17298806221103707.
[5] J. C. Liao, *Philos. Trans. R. Soc., B* **2007**, *362*, 1973.
[6] L. Li, D. Liu, J. Deng, M. J. Lutz, G. Xie, *Bioinspir. Biomim.* **2021**, *16*, 056013.
[7] K. M. Moon, J. Kim, Y. Seong, B.-C. Suh, K. Kang, H. K. Choe, K. Kim, *BMB Rep.* **2021**, *54*, 393.
[8] U. Proske, S. C. Gandevia, *Physiol. Rev.* **2012**, *92*, 161.
[9] L. Li, M. Nagy, J. M. Graving, J. Bak-Coleman, G. Xie, I. D. Couzin, *Nat. Commun.* **2020**, *11*, 1.

[10] Y. Yang, D. G. Yared, E. S. Fortune, N. J. Cowan, *Curr. Biol.* **2024**, *34*, 2118.
[11] B. J. Gibbs, O. Akanyeti, J. C. Liao, *J. Exp. Biol.* **2024**, *227*, jeb246275.
[12] A. J. Ijspeert, *Science 1979* **2014**, *346*, 196.
[13] O. Yasa, Y. Toshimitsu, M. Y. Michelis, L. S. Jones, M. Filippi, T. Buchner, R. K. Katzschmann, *Annu. Rev. Control Robot Auton. Syst.* **2023**, *6*, 1.
[14] R. Pfeifer, M. Lungarella, F. Iida, *Science 1979* **2007**, *318*, 1088.
[15] Y. Hao, Y. Cao, Y. Cao, X. Mo, Q. Huang, L. Gong, G. Pan, Y. Cao, *J. Bionic. Eng.* **2024**, *21*, 177.
[16] Y. A. Tsybina, S. Y. Gordleeva, A. I. Zharinov, I. A. Kastalskiy, A. V. Ermolaeva, A. E. Hramov, V. B. Kazantsev, *Chaos Solitons Fractals* **2022**, *165*, 112864.
[17] Y. Zhong, Z. Hong, Y. Li, J. Yu, *IEEE Trans. Rob.* **2024**, *40*, 750.
[18] J. Yu, C. Wang, G. Xie, *IEEE Trans. Ind. Electron.* **2015**, *63*, 1280.
[19] E. Angelidis, E. Buchholz, J. Arreguit, A. Rougé, T. Stewart, A. Von Arnim, A. Knoll, A. Ijspeert, *Neuromorph. Comput. Eng.* **2021**, *1*, 14005.
[20] Y. Zeng, J. Yang, Y. Yin, *Appl. Sci.* **2019**, *9*, 1711.
[21] C. G. M. Meskers, J. H. De Groot, E. De Vlugt, A. C. Schouten, *Front. Integr. Neurosci.* **2015**, *9*, 1.
[22] J. Xie, C. Li, N. Li, P. Li, X. Wang, D. Gao, D. Yao, P. Xu, G. Yin, F. Li, *Electronics* **2021**, *10*, 755.
[23] D. P. Burke, S. P. Kelly, P. De Chazal, R. B. Reilly, C. Finucane, *IEEE Trans. Neural Syst. Rehabil. Eng.* **2005**, *13*, 12.
[24] Y. Li, H. L. Wei, S. A. Billings, P. G. Sarrigiannis, *J. Neurosci. Methods* **2011**, *196*, 151.
[25] T. P. Gilmour, T. Subramanian, C. Lagoa, W. K. Jenkins, *Comput. Math Methods Med.* **2012**, *2012*, 580795.
[26] N. Aljuri, R. Marini, R. J. Cohen, *Am. J. Physiol. Heart Circ. Physiol.* **2004**, *287*, H2274.
[27] Y. Li, H. L. Wei, S. A. Billings, X. F. Liao, *Phys. Rev. E Stat. Nonlin. Soft Matter. Phys.* **2012**, *85*, 041906.
[28] W. Truccolo, U. T. Eden, M. R. Fellows, J. P. Donoghue, E. N. Brown, *J. Physiol. Org.* **2005**, *93*, 1074.
[29] F. He, Y. Yang, *Neuroscience* **2021**, *458*, 213.
[30] P. Ramdya, A. J. Ijspeert, *Sci. Robot* **2023**, *8*, eadg0279.
[31] M. A. Lebedev, M. A. L. Nicolelis, *Trends Neurosci.* **2006**, *29*, 536.
[32] R. Dong, X. Zhang, H. Li, Z. Lu, C. Li, A. Zhu, *Front. Bioeng. Biotechnol.* **2024**, *12*, 1448903.
[33] J. B. Thomas, B. Laschowski, in *2025 IEEE Inter. Conf. On Rehabilitation Robotics (ICORR)*, IEEE, Illinois **2025**, p. 1288.
[34] M. A. Montoya Martínez, R. Torres-Córdoba, E. Magid, E. A. Martínez-García, *Machines* **2024**, *12*, 124.
[35] K. Ogata, *Modern control engineering*, Prentice Hall, Upper Saddle Riverr, NJ **2010**.
[36] L. Ljung, *System Identification Theory for the User*, Prentice Hall, Upper Saddle Riverr, NJ **1999**.
[37] E. Bizzi, F. A. Mussa-Ivaldi, *Cognitive Neurosciences*, The MIT Press, Massachusetts **2009**.
[38] R. B. Stein, E. R. Gossen, K. E. Jones, *Nat. Rev. Neurosci.* **2005**, *6*, 389.
[39] A. Crespi, A. J. Ijspeert, *IEEE Trans. Rob.* **2008**, *24*, 75.
[40] R. H. Afridi, W. H. Afridi, M. Hamza, M. Wu, L.-M. Chao, Y. Zhai, L. Li, G. Xie, *Proceedings B* **2025**, *292*, 20250474.
[41] J. C. Liao, D. N. Beal, G. V. Lauder, M. S. Triantafyllou, *Science 1979* **2003**, *302*, 1566.
[42] T. Nath, A. Mathis, A. C. Chen, A. Patel, M. Bethge, M. W. Mathis, *Nat. Protocols* **2019**, *14*, 2152.
[43] P. Wellstead, *Self-tuning systems: Control and signal processing*, John Wiley & Sons, New York **1991**.
[44] S. M. Ahmad, A. Tanveer, *Ocean Eng.* **2025**, *325*, 120790.
[45] A. Tanveer, S. M. Ahmad, *Ocean Eng.* **2022**, *266*, 112836.
[46] M. Von Benzon, F. Sorensen, J. Liniger, S. Pedersen, S. Klemmensen, K. Schmidt, in *2021 IEEE European Control Conf.*, IEEE, Delft **2021**, p. 2265-2270.
[47] V. Alexandrov, D. Shatov, A. Abramenkov, A. Abdulov, in *Proc. - 2023 5th IEEE Inter. Conf. on Control Systems, Mathematical Modeling, Automation and Energy Efficiency, SUMMA 2023*, IEEE, Lipetsk **2023**, p. 76.
[48] P. L. Dos Santos, T. P. A. Perdicoúlis, B. M. Ferreira, C. Gonçalves, *IFAC-Papers OnLine* **2024**, *58*, 146.
[49] S. M. Ahmad, *Int. J. Model Identif. Control* **2015**, *24*, 75.